DOI:
10.1038/s41557-018-0014-y

Document Version
Peer reviewed version

Evidence for a vibrational phase isotope effect on the photochemistry of vision

C. Schnedermann[1,α], X. Yang[2], M. Liebel[1,£], K. M. Spillane[1,3,%], J. Lugtenburg[4], I. Fernandez[4,$], A. Valentini[5,&], I. Schapiro[6], M. Olivucci[2,5,7,*], P. Kukura[1,*], R. A. Mathies[3,*]

[1] Department of Chemistry, Physical and Theoretical Chemistry Laboratory, University of Oxford, South Parks Road, OX1 3QZ Oxford, United Kingdom.
[2] Chemistry Department, Bowling Green State University, Bowling Green, Ohio 43403, United States.
[3] Chemistry Department, University of California, Berkeley CA 94720, United States.
[4] Leiden Institute of Chemistry, Leiden University, 2300 RA Leiden, The Netherlands.
[5] Dipartimento di Biotecnologie, Chimica e Farmacia, Università di Siena, via A. Moro 2, I-53100 Siena, Siena, Italy.
[6] Fritz Haber Center for Molecular Dynamics, Institute of Chemistry, Hebrew University of Jerusalem, Jerusalem 91904, Israel.
[7] University of Strasbourg, Institute for Advanced Studies, 5, Allée du Général Rouvillois, F-67083 Strasbourg, France.

[α]*Current address: Department of Chemistry and Chemical Biology, Harvard University, 12 Oxford Street, Cambridge, Massachusetts 02138, United States.*
[£]*Current address: ICFO - Institut de Ciencies Fotoniques, The Barcelona Institute of Science & Technology, 08860 Castelldefels (Barcelona), Spain.*
[%]*Current address: Department of Physics, King's College London, London WC2R 2LS, United Kingdom*.
[$]*Current address: IFF International Flavors and Fragrances, Avda. Felipe Klein 2, 12580 Benicarló, Spain.*
[&]*Current address: Département de Chimie, Université de Liège, Allée du 6 Août, 11, 4000 Liege, Belgium.*

Abstract

Vibronic coupling is key to efficient energy flow in molecular systems and a critical component of most mechanisms invoking quantum effects in biological processes. Despite increasing evidence for coherent coupling of electronic states being mediated by vibrational motion, it is not clear how and to what degree properties associated with vibrational coherence such as phase and coupling of atomic motion can impact the efficiency of light-induced processes under natural, incoherent illumination. Here, we show that deuteration of the H_{11}-C_{11}=C_{12}-H_{12} double-bond of the 11-*cis* retinal chromophore in the visual pigment rhodopsin significantly and unexpectedly alters the photoisomerization yield while inducing only small changes in the ultrafast isomerization dynamics assignable to known isotope effects. Combination of these results with non-adiabatic molecular dynamics simulations reveals a vibrational phase-dependent isotope effect that we suggest is an intrinsic attribute of vibronically coherent photochemical processes.

The breakdown of the Born-Oppenheimer approximation separating electronic and nuclear degrees of freedom forms the basis of energy flow in molecules.[1,2] The conventionally proposed mechanism of rapid (<10 ps) condensed-phase photochemical processes is undergoing revision as a result of the combined efforts of modern ultrafast spectroscopic techniques and theoretical modeling. For multi-chromophoric systems such as light harvesting complexes, coherent vibronic coupling of electronic states has been suggested as a potential source of quantum effects influencing and possibly optimizing the outcome of energy transfer.[3–10] Other extremely rapid photochemical processes such as the primary isomerization of the retinal chromophore in rhodopsin, are now classified as intramolecular vibrationally coherent internal conversion processes through an early conical intersection (CI) allowing for the rapid formation of isomerized photoproduct irrespective of illumination conditions.[11–17] A key question that remains unanswered is whether this coherence is functionally significant.

Highly time-resolved transient grating studies of rhodopsin recently reported the sub-50 fs appearance of excited photoproduct and extracted short lifetime oscillatory vibrational features assigned to the transient excited state.[18,19] These observations suggest that the vibrational motion of key modes that make up the isomerization coordinate, like the C_{11}=C_{12} torsion and H-C_{11}=C_{12}-H hydrogen out-of-plane (HOOP) wags (also described as coupled C_{11} and C_{12} pyramidalizations) could be an important factor in determining the efficiency and outcome of the reaction. Furthermore, molecular dynamics simulations of the rhodopsin surface crossing have proposed that the phase of vibrational motions upon encountering the CI connecting the excited and ground electronic states is important for the reactivity.[13–15,20–25] In particular, recent theoretical studies on the isomerization dynamics in rhodopsin have emphasized that the degree of intramolecular vibrational coherence plays a crucial role for the quantum yield of photoproduct formation.[26,27] Despite multiple indications that the relative phase of vibrational modes may be important in rhodopsin photochemistry,[13,25,28] there is no direct experimental evidence suggesting its relevance for the chemical outcome, in particular with biologically relevant, incoherent excitation.

An informative means to test the reactive influence of vibrational modes and their phase relationship at the CI involves isotopic labeling. Isotopes have traditionally been employed to study reaction mechanisms

through primary kinetic isotope effects where the isotopomer is transferred, such as in the light-driven proton transfer in green-fluorescent protein.[29,30] The primary kinetic isotope effect arises from the change in the zero-point energy for the heavier atom, but even larger effects have been reported when tunneling plays a role in the reaction mechanism.[30] In the context of visual photochemistry, early studies suggested a primary kinetic isotope effect associated with chromophore proton or hydrogen transfer, but these models have not been sustained.[31,32]

To examine the effect of isotopic substitution on the photochemistry of vision, we synthesized three modified 11-*cis* retinal analogues (11-D, 12-D and 11,12-D_2) and regenerated these chromophores in the opsin protein (Fig. 1). We then characterized the isomerization quantum yield using a continuous-wave light source[33–35] and the isomerization kinetics by recording the dynamic appearance of the photoproduct using ultrafast transient absorption spectroscopy.[16,36] Isotopic substitution had a large effect on the photochemical quantum yield, which is dictated by the efficiency of internal conversion through the CI from the excited-state 11-*cis* reactant to the all-*trans* photoproduct. The effect of isotopic substitution on the photoisomerization kinetics was, however, less pronounced and followed the trend expected for known isotope effects. These results, coupled with non-adiabatic molecular dynamics simulations, suggest a novel isotope effect where mass-induced changes in vibrational phase and thereby mode-specific vibrational coupling alter the reaction efficiency of a vibronically coherent photochemical reaction.

Results and Discussion

Isomerization quantum yield

Native and 11,12-H_2 regenerated rhodopsin exhibited statistically indistinguishable isomerization quantum yields of 0.63 (±0.01) and 0.65 (±0.01), respectively, demonstrating that retinal regeneration did not alter the system (Fig. 2). The 11,12-D_2 derivative exhibited a quantum yield of 0.69 (±0.01), which is higher compared to the native and regenerated chromophore. In contrast, the 11-D and 12-D isotopomers, with just a single isotopic substitution, had substantially lower quantum yields of 0.45 (±0.01) and 0.48 (±0.01), respectively. This surprising yield reduction in view of the increase for 11,12-D_2 is statistically significant beyond

experimental error. The protonated 11-*cis* chromophore in solution exhibited an even lower quantum yield of 0.19 (±0.04) outside the protein pocket.[37] These results evidence an anomalous isotope effect where symmetric deuteration of the isomerizing bond produces a higher isomerization quantum yield while asymmetric isotopic substitution significantly lowers the yield.

Transient absorption spectroscopy and dynamics

The differences in isomerization yield could in principle be explained by a non-trivial dependence of the reaction rate on isotopic substitution, especially given the proposed involvement of hydrogen wagging motion in the reaction.[12,13,16,18,23,25] We thus recorded the appearance of the photoproduct of native rhodopsin and its isotopic derivatives using broadband transient absorption spectroscopy after excitation at the rhodopsin absorption maximum (498 nm) with a 20 fs pulse. We then followed the growth of the photoinduced absorption in the region from 545-616 nm, indicative of the formation of the primary photoproduct, for each derivative including native and 11,12-H_2 regenerated rhodopsin (Fig. 3a). All traces exhibited the expected features known for rhodopsin photochemistry: an oscillatory coherent artifact near zero pump-probe delay,[38] a delayed growth of the photoproduct signal that is complete by ~200 fs[11,39] and weak modulations of the electronic signal for longer time delays caused by coherent nuclear motion of the photoproduct.[16,17] The coherent artifacts are nearly identical for all derivatives with any variations caused by the different optical densities available for the five samples. The most prominent differences in the traces are restricted to the appearance of the vibrational coherence superimposed on the electronic signal in the 300-500 fs window, as expected for changes in vibrational frequencies caused by isotopic substitution. The overall similarity of the electronic dynamics suggested by the ultrafast appearance of the photoproduct signal continued throughout the entire probed region (500-900 nm, Supplementary Fig. 1).

To more carefully quantify the dynamics of photoproduct formation, we fitted the transients in Fig. 3a to a sum of a coherent artifact contribution and a mono-exponential decay function convolved with a Gaussian function describing formation of the photoproduct (Supplementary Figs. 2-4).[40] This approach allowed us to define the time delay when pump and probe pulses arrive at the sample ($t_{0,CA}$) independently of the time delay of photoproduct formation ($t_{0,PIA}$). The difference ($t_{0,PIA}$ - $t_{0,CA}$) provides an internally referenced measure

of the lag time for photoproduct formation, which can be taken as representative of the time it takes for the excited-state population to reach the CI (Fig. 3b). Furthermore, the rise time of the photoproduct formation (σ_{PIA}) provides a measure of how quickly the excited state is depopulated once the CI is reached (Fig. 3c). We refer the reader to section 2 of the Supplementary Information for a more detailed analysis and discussion of the fitting procedure.

The retrieved average lag time is 150.6 ± 5.2 fs but the individual traces show subtle variations across the isotopomers (Fig. 3b). Native and 11,12-H_2 regenerated rhodopsin are expected to show the same value but differ by 3.2 fs. While we cannot rule out that the reconstitution process introduces this difference, we attribute this difference to systematic errors not accounted for by our fitting model, putting a lower limit to the precision with which we can quantify differences between the isotopomers (see Supplementary Fig. 2-4). Using the same procedure, we find that the lag time for 11,12-D_2 increases by 9.1 fs. The 11-D isotopomer exhibits similar dynamics to 11,12-D_2 (increase by 7.3 fs) while 12-D is indistinguishable from native rhodopsin. The retrieved average photoproduct formation rise time of 29.3 ± 3.4 fs (Fig. 3c) agrees with recent transient grating measurements on rhodopsin.[18] The trend observed for the rise times differs significantly compared to the lag times observed in Fig. 3b as all isotopomers apart from 11-D show identical values within error bounds. We remark, however, that any fitting model can only yield strictly comparable parameters under the assumption that all samples were measured with the same optical density, which was not possible for 11-D (see Methods). Consequently, contributions from vibrational coherences and different signal-to-noise levels are likely to differentially affect the retrieved kinetic parameters.

Our analysis suggests a weak dependence of the photochemical dynamics upon isotopic substitution manifested in the delayed appearance (lag time) of the photoproduct formation for deuterated isotopomers relative to native rhodopsin. This delay is correlated with the degree of isotopic substitution and is expected based on mixing of the HOOP mode with the C_{11}=C_{12} torsional mode whose frequency primarily determines the time it takes to reach the CI. A higher isotope mass will consequently result in a lower torsional frequency and a retardation of the reaction speed with our analysis revealing an upper bound for this retardation of ~7% for 11,12-D_2 relative to the average of native and 11,12-H_2 regenerated rhodopsin. Critically, the

variations in dynamic parameters (Fig. 3b, c) are small compared to changes in isomerization quantum yields which range from -30% to +8% (Fig. 2) and there appears to be no correlation between these observables (see Supplementary Fig. 5). The C_{11}-H or C_{12}-H HOOP motion is therefore not rate limiting for the reaction as might be expected based on a Landau-Zener-type surface tunneling mechanism.[41,42] Traditional primary or secondary kinetic isotope effects including tunneling[30] can be ruled out as well because the quantum yield for the 11,12-D_2 derivative is higher and heavy isotope effects on the zero-point energy or on tunneling probability generally result in lower reaction rates.

These results can be understood by adopting an intramolecular vibrationally coherent picture of rhodopsin's reactive internal conversion, which considers the nature and relative timing and phasing of the various nuclear motions within a single molecule. The extremely rapid isomerization event reduces the overall reaction coordinate in rhodopsin to critical displacements along a localized backbone torsion and a HOOP motion, with surface hopping restricted to a relatively narrow range of torsional angles around 90 degrees.[13,25] A local isomerizing twist about the C_{11}=C_{12} double bond is achieved through a correctly phased motion of the C_{10}-C_{11}=C_{12}-C_{13} torsion and the corresponding anti-symmetric H-C_{11}=C_{12}-H torsion, related to the HOOP coordinate, at the CI. A successful isomerization reaction thus requires a cooperative effect of both vibrational degrees of freedom in a well-defined manner.

Quantum-chemical trajectory calculations

To obtain deeper insight into the phase relationship and role of these modes, we carried out non-adiabatic molecular dynamics simulations for all studied isotopomers using a multiconfigurational-QM/MM rhodopsin model featuring a computationally more affordable five double-bond chromophore (Fig. 4a).[13,24] The excited-state lifetime and quantum yield of each isotopomer were computed by propagating 400 semi-classical trajectories starting with initial conditions corresponding to a room-temperature Boltzmann distribution. The simulated quantum yields paralleled the experimentally observed trend (increase for 11,12-D_2, decrease for 11-D and 12-D) as well as the weaker isotope-dependent trend in the lag times in agreement with previous full-chromophore studies (Table 1).[11,13]

Motivated by this agreement between experiment and theory, we investigated the simulated trajectories to extract general trends for all isotopomers governing the underlying mechanisms. Upon analyzing the population decay we consistently observed an oscillatory behavior showing initially alternating 'reactive' (formation of *trans*-photoproduct) and 'unreactive' (formation of *cis*-reactant) waves associated with different subsets of the decaying population (Fig. 4b). The subsets corresponded to distinct phases of the torsion (α) and HOOP (δ_{op}) coordinate (Fig. 4a). It is instructive to define an effective coordinate $\tau = \alpha - \frac{\delta_{op}}{2}$, which is proportional to the overlap between the π-orbitals involved in the breaking and reconstitution of the C_{11}=C_{12} double bond (Fig. 4a, right hand side).[13] We found that the 'reactive' or 'unreactive' direction is best described by considering the velocity of the angle τ at the CI, where a negative τ velocity leads to *trans*-photoproduct formation (Fig. 4c, orange) while a positive τ velocity results in *cis*-reactant formation (Fig. 4c, blue). Further examining the individual components of the τ motion revealed a similar α component in reactive and unreactive trajectories, rendering the velocity of δ_{op} (i.e. of the HOOP coordinate) the decisive factor determining the sign of the τ velocity and therefore the quantum yield of the reaction. As highlighted in Fig. 4d, reactive and unreactive trajectories approach the CI at approximately the same α velocity in both cases with α moving towards more negative values. Successful *trans*-photoproduct formation occurs, however, only if δ_{op} moves in the opposite direction to α, i.e. towards more positive values, to achieve a counterclockwise skeletal twisting motion (orange trajectory), while *cis*-reactant reformation is observed if δ_{op} moves in the same direction as α, i.e. towards more negative values (blue trajectory).

Following these findings, we can now reconcile the discrepancy arising between the modest changes in reaction rates and the non-monotonous trend in isomerization quantum yields for rhodopsin isotopomers. Partial deuteration of the retinal backbone has only a small effect on the torsional mode progression and consequently on the movement of the ground and excited electronic states towards the CI, because the torsion is predominantly localized on the carbon framework.[24,43] Since the surface hopping probability is directly linked to the evolution of this torsion to values close to 90 degrees, no significant kinetic changes are expected upon deuteration in agreement with our experimental and theoretical observation of a weak isotope-dependence on the excited-state lifetime. The main difference between the isotopomers used here is that the C_{11}-H and C_{12}-H wags are coupled for native 11,12-H_2 rhodopsin and for 11,12-D_2, resulting in the

formation of symmetric and anti-symmetric HOOP vibrations where the two hydrogen (deuterium) displacements maintain a specific phase relationship with the carbon torsional coordinate until the molecule decays via the CI. In this context, di-deuteration provides a slightly more suitable phase-matching of the HOOP to the torsional motion, resulting in an increase in the isomerization quantum yield (compare Supplementary Fig. 12 and 13). When a single position is deuterated, however, that coupling is reduced resulting in more isolated C-H and C-D out-of-plane wags associated with a less well-phased HOOP motion.[44] Consequently, a single deuteration significantly alters the phase relationship between the C-H and C-D wagging motions and ultimately the torsion at the CI, thereby inhibiting photoproduct formation.

Two-mode harmonic model

To understand how an increasing level of deuteration of the C_{11}=C_{12} double bond can result in the observed non-monotonous quantum yield trend (increase for 11,12-D_2, decrease for 11-D and 12-D) for the vibrationally coherent photoisomerization in rhodopsin, we constructed a minimal two-mode harmonic model with frequency parameters (ω_α and $\omega_{\delta op}$) derived from the simulations (see Supplementary Information, section 7). The model contains a torsional mode with ω_α = 83 cm^{-1} and a HOOP mode with an isotope-dependent $\omega_{\delta op}$ = 953 cm^{-1}, 855 cm^{-1} or 725 cm^{-1} for 11,12-H_2, 11-D/12-D or 11,12-D_2, defined by equations (1) and (2).

$$\alpha = A_\alpha cos[\omega_\alpha t] + B \qquad (1)$$

$$\delta_{op} = A_{\delta op} cos\left[\omega_{\delta op} t + C\right] \qquad (2)$$

The amplitude parameters A_α and $A_{\delta op}$ are also extracted from the 400 calculated trajectories and kept constant in all cases. The B and C coefficients represent initial conditions (t = 0) and are obtained from the simulated Boltzmann distribution of each isotopomer. Each trajectory computed using equations (1) and (2) represents the coherent dynamics of a population subset defined by the B and C values.

The modeled time evolution of α, δ_{op} and the resulting τ value for specific B and C values of the 11,12-H_2 isotopomer are illustrated in Fig. 5a. The normalized fraction of decayed trajectories at each time point is calculated to be proportional to the velocity of τ multiplied by the value of a reference Gaussian function (derived from the simulations) and a population decay factor, which represents the decay probability (Fig. 5a, gray shaded area). The population subset of 11,12-H_2 decays in three distinct waves (Fig. 5a, bottom), namely two reactive (orange) and one unreactive (blue) wave, showing the same oscillatory character of the population decay found in the full simulation (Fig. 4b). In fact, the short time separation between the first reactive and the unreactive wave and the larger time separation between the two successive reactive waves in Fig. 5a roughly matches the time separations between the corresponding reactive and unreactive maxima found in the simulation (Fig. 4b). These observations indicate that the oscillations in the population decay for both the reactive and unreactive sub-populations are present in a basic 2D model and must results from the superposition of trajectory subsets with the same features but displaying decay waves at different times and amplitudes. The modeling of trajectories characterized by different B and C values and/or $\omega_{\delta op}$ value indicates that the above conclusions are general.

The origin of the modeled decay waves can be understood by considering the corresponding temporal evolution of the torsion and HOOP coordinates (Fig. 5b). At ~70 fs delay (compare Fig. 5a and 5b), the trajectory enters the decay region. Initially the trajectory shows a positive velocity of δ_{op} and the corresponding decay leads to photoproduct formation (compare Fig. 5b to Fig. 4d). At the turning point, the trajectory inverts its direction still remaining in the decay region and thus leading to reactant formation upon decay. At ~85 fs, the trajectory exits the decay region halting a population decay. Just before 100 fs, however, the trajectory re-enters the decay region with a positive velocity of δ_{op} leading to a second wave of photoproduct formation, which is stopped after ~110 fs.

According to the above model the change in the overall quantum yield upon isotopic labeling depends on three factors characterizing each population subset: the initial conditions, the evolution of the phase relationship between δ_{op} and α and the magnitude of the dephasing of the C_{11}-H and C_{12}-H wags. We find that the deviation of the average δ_{op} of the simulated trajectories, $d(\delta_{op}^{AV})/dt$, of asymmetrically deuterated

isotopomers is more sensitive to the value of the initial conditions than that of their symmetric counterparts. This is reflected by the deviation of the simulated population dynamics from a trajectory released from the Franck-Condon point with no velocities (see Supplementary Fig. 12). More specifically, the 11,12-H_2 and 11,12-D_2 populations follow rather closely such trajectory revealing that the corresponding motion is dominated by the structure of the excited-state potential energy surface rather than by the initial velocities. This condition would guarantee a high degree of vibrational coherence. In contrast, the 11-D and 12-D populations display much larger deviations suggesting a more de-phased motion and a lesser degree of vibrational coherence. Thus, despite being intrinsically dependent on a frequency change occurring upon isotopic substitution, the observed/simulated isotope effect should be described as a vibrational phase isotope effect, since it relies on the dynamic phase relationship achieved at the CI by the fundamental vibrational modes involved in the reaction coordinate. It is thus distinctly different from the often-employed primary and secondary kinetic isotope effects, which operate after dephasing has taken place.

Conclusion

We have shown experimentally and theoretically that deuteration along the isomerizing double-bond of the retinal chromophore in rhodopsin causes a significant and unanticipated pattern of isomerization quantum yield changes while inducing only modest perturbations of the kinetics in line with known isotope effects. The lack of correlation between these two experimental observables points towards the existence of a novel vibrational phase isotope effect that could be functionally important for other ultrafast and vibrationally coherent processes.[45] Although illustrated here for rhodopsin photochemistry, vibrational phase isotope effects should be a general and powerful approach for revealing the importance of vibronic coupling in ultrafast light induced processes, such as Förster or Dexter energy transfer, electron transfer, ultrafast internal conversion or proton transfers. The fact that this vibrational phase isotope effect is manifested in the quantum yield measured with incoherent light demonstrates the importance of intramolecular multimode vibrational coherence in photochemical reactions, irrespective of the illumination conditions.[40,41] Finally, we remark that the observed phase dependence is most likely not only a classical effect but intrinsically linked to the quantum nature of the reaction in a non-adiabatic region of the potential energy

surface. In rhodopsin, the vibrational phase modulations affecting the quantum yield also have an impact on the electron re-coupling, a purely quantum mechanical process, which allows for the C_{11}=C_{12} double bond reconstitution. The vibrational isotope effect thus opens new avenues for studying ultrafast energy flow in vibronic processes beyond the Born-Oppenheimer approximation.

Acknowledgments

We acknowledge support from the National Eye Institute for providing 11-*cis* retinal used to make the 11,12-H_2 regenerated rhodopsin sample. P.K. was supported by the EPSRC (EP/K006630/1). M.O. is supported by the NSF (CHE-1710191) and HFSP (RGP0049/2012) and also thanks the Ohio Supercomputer Center for computer time. I.S. is supported by the ERC Starting Grant 'PhotoMutant' (678169). This work was supported in part by the Mathies Royalty Fund.

Author Contributions

R.A.M. and J.L. conceived the project. P.K., C.S. and M.L. designed all experiments and analyzed the data. J.L. and I.F. synthesized the isotopomers. M.O. and X.Y. carried out the molecular dynamics simulations and developed the proposed theoretical model. I.S. and A.V. wrote the isotope simulation code. K.M.S. prepared the rhodopsin samples for all measurements. C.S., P.K., M.O. and R.A.M. wrote the manuscript with contributions from all other authors.

Competing financial interests

The authors declare no competing financial interests.

Corresponding authors

*ramathies@berkeley.edu; philipp.kukura@chem.ox.ac.uk; massimo.olivucci@unisi.it

Methods

Sample Preparation

Rhodopsin samples were prepared in a 100 mM sodium phosphate buffer (pH 7.1% Ammonyx-LO) as described by Eyring et al.[44] with optical densities at 498 nm of: OD(native rhodopsin) = 3.0, OD(11,12-H_2 regenerated) = 3.4, OD(11,12-D_2) = 4.2, OD(11-D) = 0.54, OD(12-D) = 1.3.

Ultrafast Spectroscopy

The experimental setup has been described by Liebel et al.[36] Briefly, pulses were delivered by a Pharos-6W amplifier system (LightConversion, 1030 nm, 180 fs, 1.05 W at 1 kHz). A small fraction was split off to generate the white light probe pulses (500-900 nm) in a 3 mm sapphire crystal. Pump pulses were generated in a home-built non-collinear optical parametric amplifier as detailed elsewhere,[46] and compressed to 20 fs (transform-limit) with a set of chirped mirrors (Layertec).

Samples were flowed through a 500 μm path length flowcell (120 μm windows) by a peristaltic pump at a rate sufficient to ensure replenishment of the sample between consecutive laser shots. Furthermore, we added NH_2OH (0.2 mM) to degrade subsequent photointermediates. Pump and probe focus diameters were 65 and 44 μm with corresponding pulse energies set to 20 nJ and 2.5 nJ, respectively. The optical densities of the samples at 500 nm in the sample cell were: OD(rhodopsin) = 0.15, OD(regenerated) = 0.17, OD(11,12-D_2) = 0.21, OD(11-D) = 0.027, OD(12-D) = 0.065.

Quantum Yield Measurements

Continuous-wave laser output (532 nm, 0.6 mW) was passed through a Glan-Taylor polarizer (Thorlabs), narrow-band filtered (532 nm, FWHM = 10 nm, Thorlabs) and attenuated to 1 μW before being split by a 50:50 beamsplitter (Thorlabs) into a reference and a sample beam. The sample beam illuminated a 1 cm path length quartz cuvette. Both reference and transmitted sample beams were subsequently detected with an EMCCD (Andor iXon3 860). Integration of the detected spots provided (referenced) bleaching curves (corrected for 4.5% back-reflection of the cuvette), which were analyzed using the established protocol.[33,34]

Samples were diluted with buffer solution (100 mM sodium phosphate buffer, pH 7.1% Ammonyx-LO) to an OD at 498 nm of 0.3 and NH_2OH was added to rapidly degrade later photointermediates. Each sample was stirred constantly during the measurement and illuminated for 20 min corresponding to a bleaching of <15 % of the initial molecules. The quantum yield of the 11-*cis* chromophore in methanol was measured according to the procedure described by Sovdat et al.[37,47]

Statistical significance (n=4) was determined based on a *t*-test at 99% confidence interval to yield p(11,12-H_2 regenerated)=0.111, t(11,12-H_2 regenerated)=1.867; p(11,12-D_2)=6.9x10^{-4}, t(11,12-D_2)=9.694; p(11-D)<1x10^{-5}, t(11-D)=27.014; p(12-D)=2.8x10^{-5}, t(12-D)=11.342.

Simulations

The employed QM/MM model was constructed starting from the 2.2 Å resolution crystallographic structure of bovine rhodopsin (PDB code: 1U19)[48] and following the protocol reported by Luk et al.[49] All retinylidene, NH and CεH_3 atoms linked to the C_δ atom of the Lys296 side-chain were included in the QM subsystem. The remaining atoms formed an MM subsystem described by the AMBER94 force field.[50] After QM/MM geometry optimization at the CASSCF(12,12)/6-31G*/Amber level, a more computationally affordable model featuring a chromophore with five conjugating double bonds was generated following the protocol described by Manathunga et al.[51] and geometrically optimized at the CASSCF(10,10)/6-31G*/Amber level. This model was then used to simulate a room-temperature Boltzmann-like distribution and extract 400 initial conditions for each isotopomer at room temperature.[51] Finally non-adiabatic population dynamics at the same CASSCF(10,10)/6-31G*/Amber level were performed using the stochastic Tully surface-hop method.[52,53] All calculation were run using the Molcas[54]/Tinker[55] interface suitably modified to account for the deuterium mass. More details are provided in the Supplementary Information, sections 4-7.

Data availability

The authors declare that the data supporting the findings of this study are available within the main article and the Supplementary Information. Additional data are available from the corresponding author upon request or can be accessed free of charge at http://ora.ox.ac.uk.

References

1. Born, M. & Oppenheimer, R. Zur Quantentheorie der Molekeln. *Ann. Phys.* **389,** 457–484 (1927).

2. Butler, L. J. Chemical reaction dynamics beyond the Born-Oppenheimer approximation. *Annu. Rev. Phys. Chem.* **49,** 125–171 (1998).

3. Brixner, T. *et al.* Two-dimensional spectroscopy of electronic couplings in photosynthesis. *Nature* **434,** 625–628 (2005).

4. Engel, G. S. *et al.* Evidence for wavelike energy transfer through quantum coherence in photosynthetic systems. *Nature* **446,** 782–786 (2007).

5. Lee, H., Cheng, Y.-C. & Fleming, G. R. Coherence dynamics in photosynthesis: protein protection of excitonic coherence. *Science* **316,** 1462–1465 (2007).

6. Romero, E. *et al.* Quantum coherence in photosynthesis for efficient solar-energy conversion. *Nat. Phys.* **10,** 676–82 (2014).

7. Dostál, J., Pšenčík, J. & Zigmantas, D. In situ mapping of the energy flow through the entire photosynthetic apparatus. *Nat. Chem.* **8,** 705–710 (2016).

8. Delor, M. *et al.* On the mechanism of vibrational control of light-induced charge transfer in donor–bridge–acceptor assemblies. *Nat. Chem.* **7,** 689–695 (2015).

9. Lim, J. S., Lee, Y. S. & Kim, S. K. Control of Intramolecular Orbital Alignment in the Photodissociation of Thiophenol: Conformational Manipulation by Chemical Substitution. *Angew. Chemie Int. Ed.* **47,** 1853–1856 (2008).

10. Lim, J. S. & Kim, S. K. Experimental probing of conical intersection dynamics in the photodissociation of thioanisole. *Nat. Chem.* **2,** 627–632 (2010).

11. Polli, D. *et al.* Conical intersection dynamics of the primary photoisomerization event in vision. *Nature* **467,** 440–443 (2010).

12. Kukura, P., McCamant, D. W., Yoon, S., Wandschneider, D. B. & Mathies, R. A. Structural observation of the primary isomerization in vision with femtosecond-stimulated Raman. *Science* **310,** 1006–1009 (2005).

13. Schapiro, I. *et al.* The ultrafast photoisomerizations of rhodopsin and bathorhodopsin are modulated by bond length alternation and HOOP driven electronic effects. *J. Am. Chem. Soc.* **133,** 3354–3364 (2011).

14. Frutos, L. M., Andruniów, T., Santoro, F., Ferré, N. & Olivucci, M. Tracking the excited-state time evolution of the visual pigment with multiconfigurational quantum chemistry. *Proc. Natl. Acad. Sci. U. S. A.* **104,** 7764–7769 (2007).

15. Strambi, A., Coto, P. B., Frutos, L. M., Ferré, N. & Olivucci, M. Relationship between the excited state relaxation paths of rhodopsin and isorhodopsin. *J. Am. Chem. Soc.* **130,** 3382–3388 (2008).

16. Schnedermann, C., Liebel, M. & Kukura, P. Mode-Specificity of Vibrationally Coherent Internal Conversion in Rhodopsin during the Primary Visual Event. *J. Am. Chem. Soc.* **137,** 2886–2891 (2015).

17. Wang, Q., Schoenlein, R. W., Peteanu, L. A., Mathies, R. A. & Shank, C. V. Vibrationally coherent photochemistry in the femtosecond primary event of vision. *Science* **266,** 422–424 (1994).

18. Johnson, P. J. M. *et al.* Local vibrational coherences drive the primary photochemistry of vision. *Nat.*

Chem. **7,** 980–986 (2015).

19. Mathies, R. A. Photochemistry: A coherent picture of vision. *Nat. Chem.* **7,** 945–947 (2015).

20. Garavelli, M., Celani, P., Bernardi, F., Robb, M. A. & Olivucci, M. The $C_5H_6NH_2^+$ Protonated Shiff Base: An ab Initio Minimal Model for Retinal Photoisomerization. *J. Am. Chem. Soc.* **119,** 6891–6901 (1997).

21. Sinicropi, A., Migani, A., De Vico, L. & Olivucci, M. Photoisomerization acceleration in retinal protonated Schiff-base models. *Photochem. Photobiol. Sci.* **2,** 1250 (2003).

22. Garavelli, M. *et al.* Photoisomerization Path for a Realistic Retinal Chromophore Model: The Nonatetraeniminium Cation. *J. Am. Chem. Soc.* **120,** 1285–1288 (1998).

23. Gozem, S. *et al.* Mapping the Excited State Potential Energy Surface of a Retinal Chromophore Model with Multireference and Equation-of-Motion Coupled-Cluster Methods. *J. Chem. Theory Comput.* **9,** 4495–4506 (2013).

24. Weingart, O. & Garavelli, M. Modelling vibrational coherence in the primary rhodopsin photoproduct. *J. Chem. Phys.* **137,** 22A523 (2012).

25. Weingart, O. *et al.* Product formation in rhodopsin by fast hydrogen motions. *Phys. Chem. Chem. Phys.* **13,** 3645–3648 (2011).

26. Duan, H.-G., Miller, R. J. D. & Thorwart, M. Impact of Vibrational Coherence on the Quantum Yield at a Conical Intersection. *J. Phys. Chem. Lett.* **7,** 3491–3496 (2016).

27. Qi, D.-L., Duan, H.-G., Sun, Z.-R., Miller, R. J. D. & Thorwart, M. Tracking an electronic wave packet in the vicinity of a conical intersection. *J. Chem. Phys.* **147,** 74101 (2017).

28. Mathies, R. A. & Lugtenburg, J. Chapter 2 The primary photoreaction of rhodopsin. *Handb. Biol. Phys.* **3,** 55–90 (2000).

29. Laptenok, S. P. *et al.* Complete Proton Transfer Cycle in GFP and Its T203V and S205V Mutants. *Angew. Chemie Int. Ed.* **54,** 9303–9307 (2015).

30. Klinman, J. P. & Kohen, A. Hydrogen Tunneling Links Protein Dynamics to Enzyme Catalysis. *Annu. Rev. Biochem.* **82,** 471–496 (2013).

31. Peters, K., Applebury, M. L. & Rentzepis, P. M. Primary photochemical event in vision: proton translocation. *Proc. Natl. Acad. Sci. U. S. A.* **74,** 3119–3123 (1977).

32. Fransen, M. R. *et al.* Structure of the chromophoric group in bathorhodopsin. *Nature* **260,** 726–727 (1976).

33. Kim, J. E., Tauber, M. J. & Mathies, R. A. Wavelength Dependent *Cis-Trans* Isomerization in Vision. *Biochemistry* **40,** 13774–13778 (2001).

34. Kochendoerfer, G. G., Verdegem, P. J., van der Hoef, I., Lugtenburg, J. & Mathies, R. A. Retinal analog study of the role of steric interactions in the excited state isomerization dynamics of rhodopsin. *Biochemistry* **35,** 16230–16240 (1996).

35. Lin, S. W. *et al.* Vibrational Assignment of Torsional Normal Modes of Rhodopsin: Probing Excited-State Isomerization Dynamics along the Reactive C_{11}=C_{12} Torsion Coordinate. *J. Phys. Chem. B* **102,** 2787–2806 (1998).

36. Liebel, M., Schnedermann, C., Wende, T. & Kukura, P. Principles and Applications of Broadband Impulsive Vibrational Spectroscopy. *J. Phys. Chem. A* **119,** 9506–9517 (2015).

37. Bassolino, G. *et al.* Barrierless Photoisomerization of 11-*cis* Retinal Protonated Schiff Base in Solution. *J. Am. Chem. Soc.* **137,** 12434–12437 (2015).

38. Kovalenko, S. A., Dobryakov, A. L., Ruthmann, J. & Ernsting, N. P. Femtosecond spectroscopy of condensed phases with chirped supercontinuum probing. *Phys. Rev. A* **59,** 2369–2384 (1999).

39. Schoenlein, R. W., Peteanu, L. A., Mathies, R. A. & Shank, C. V. The first step in vision: femtosecond isomerization of rhodopsin. *Science* **254,** 412–415 (1991).

40. Dobryakov, A. L. *et al.* Femtosecond pump/supercontinuum-probe spectroscopy: Optimized setup and signal analysis for single-shot spectral referencing. *Rev. Sci. Instrum.* **81,** 113106 (2010).

41. Zener, C. Non-Adiabatic Crossing of Energy Levels. *Proc. R. Soc. A Math. Phys. Eng. Sci.* **137,** 696–702 (1932).

42. Landau, L. D. On the theory of transfer of energy at collisions II. *Phys. Z. Sowjetunion* **2,** 7 (1932).

43. Ockenfels, A., Schapiro, I. & Gärtner, W. Rhodopsins carrying modified chromophores – the 'making of', structural modelling and their light-induced reactivity. *Photochem. Photobiol. Sci.* **15,** 297–308 (2016).

44. Eyring, G., Curry, B., Broek, A., Lugtenburg, J. & Mathies, R. A. Assignment and interpretation of hydrogen out-of-plane vibrations in the resonance Raman spectra of rhodopsin and bathorhodopsin. *Biochemistry* **21,** 384–393 (1982).

45. Gozem, S., Luk, H. L., Schapiro, I. & Olivucci, M. Theory and Simulation of the Ultrafast Double-Bond Isomerization of Biological Chromophores. *Chem. Rev.* **117,** 13502–13565 (2017).

46. Liebel, M., Schnedermann, C. & Kukura, P. Sub-10-fs pulses tunable from 480 to 980 nm from a NOPA pumped by an Yb:KGW source. *Opt. Lett.* **39,** 4112–4115 (2014).

47. Sovdat, T. *et al.* Backbone modification of retinal induces protein-like excited state dynamics in solution. *J. Am. Chem. Soc.* **134,** 8318–8320 (2012).

48. Okada, T. *et al.* The Retinal Conformation and its Environment in Rhodopsin in Light of a New 2.2Å Crystal Structure. *J. Mol. Biol.* **342,** 571–583 (2004).

49. Luk, H. L. *et al.* Modulation of thermal noise and spectral sensitivity in Lake Baikal cottoid fish rhodopsins. *Sci. Rep.* **6,** 38425 (2016).

50. Cornell, W. D. *et al.* A Second Generation Force Field for the Simulation of Proteins, Nucleic Acids, and Organic Molecules. *J. Am. Chem. Soc.* **117,** 5179–5197 (1995).

51. Manathunga, M. *et al.* Probing the Photodynamics of Rhodopsins with Reduced Retinal Chromophores. *J. Chem. Theory Comput.* **12,** 839–850 (2016).

52. Tully, J. C. Molecular dynamics with electronic transitions. *J. Chem. Phys.* **93,** 1061–1071 (1990).

53. Granucci, G. & Persico, M. Critical appraisal of the fewest switches algorithm for surface hopping. *J. Chem. Phys.* **126,** 134114 (2007).

54. Aquilante, F. *et al.* Molcas 8: New capabilities for multiconfigurational quantum chemical calculations across the periodic table. *J. Comput. Chem.* **37,** 506–541 (2016).

55. Ponder, J. W. & Richards, F. M. Tinker Molecular Modeling Package. *J. Comput. Chem.* **8,** 1016–1024 (1987).

Figure captions

Figure 1. Native and isotopically labelled 11-*cis* retinal protonated Schiff base chromophores in rhodopsin studied in this work.

Figure 2. Isomerization quantum yields for native, 11,12-H_2 regenerated and isotopically labelled retinal chromophores in rhodopsin obtained at an excitation wavelength of 532 nm. Grey - symmetrically substituted, orange - asymmetrically substituted. The quantum yields are compared to the free chromophore in methanol solution (blue,*) obtained using a different procedure (see Methods).

Figure 3. Transient absorption measurements and corresponding fitting results of rhodopsin regenerated with retinal chromophores with different patterns of isotopic substitution about the isomerizing C_{11}=C_{12} double bond. **a**, Normalized differential absorbance averaged over the full photoproduct absorption band (545-616 nm, grey circles) and corresponding fits (black dashed). The photoproduct rise has been highlighted in orange for clarity. Traces were normalized to the maximum absorption feature occurring at a time delay of 200 fs. Time delays <75 fs (grey shaded) have been manually scaled as indicated to show coherent artifact and photoproduct signal contributions on the same scale for visual purposes. **b**, Retrieved lag (or delay) time before photoproduct formation and **c**, Rise time of the photoproduct after the lag period. Error bars represent one standard deviation. See Supplementary Information, section 2, for detailed trace alignment and fitting procedure.

Figure 4. Simulated excited-state isomerization dynamics of bovine rhodopsin. a, Dihedral angles defining the chromophore double-bond torsion (α) and hydrogen-out-of-plane (δ_{op}) coordinates. The relationship between the 'overlap' coordinate (τ) and the π-orbitals (green) responsible for double bond reconstitution is schematically illustrated on the right. hδ_{op}(H_{11}) is defined as the dihedral angle between the $H_{11}C_{11}C_{12}$ and

$C_{10}C_{11}C_{12}$ planes and $h\delta_{op}(H_{12})$ is defined as the dihedral angle between the $H_{12}C_{11}C_{12}$ and $C_{11}C_{12}C_{13}$ planes in such a way that the relationship $\delta_{op} = h\delta_{op}(H_{11}) + h\delta_{op}(H_{12})$ is satisfied. **b**, Oscillatory character of the excited-state population decay for both the reactive and unreactive sub-populations. **c**, Distribution of the τ velocities at the decay point (CI) for the reactive and unreactive sub-populations. Negative and positive τ velocities correlate with reactive (orange) and unreactive (blue) events, respectively. **d**, Representative reactive and unreactive trajectories showing that the sign of the τ velocity is determined by the sign of the δ_{op} velocity. The two straight dashed lines give the corresponding values of τ for the reactive (orange) and unreactive (blue) trajectory.

Figure 5. 2D-modeling of simulated rhodopsin population dynamics. a, Graphical representation of the α and δ_{op} periodic functions and Gaussian decay region defining the model. The alternating reactive and nonreactive population decay events produced by the model are projected below. **b**, Origin of the reactive (orange) and nonreactive (blue) decay events in terms of trajectory segments characterized by an increase and decrease of δ_{op} while α is monotonically increasing. The shaded area between τ = -76 and τ = -96 degrees defines the decay region (gray shaded) centered along the collection of CI points forming the intersection space (black dashed line).[15]

Tables

Table 1. Comparison of experimental and simulated photoproduct kinetics and quantum yields for rhodopsin isotopomers. All indicated errors refer to one standard deviation.

		11,12-H_2[2]	**11,12-D_2**	**11-D**	**12-D**
Experiment	lag time[1] (fs)	147.7 ± 1.0	156.8 ± 1.9	155.0 ± 0.86	148.8 ± 1.1
	quantum yield	0.63 ± 0.01	0.69 ± 0.01	0.45 ± 0.02	0.48 ± 0.01
Simulation	hop time[3] (fs)	100 ± 31	113 ± 41	100 ± 35	93 ± 35
	quantum yield	0.69	0.70	0.61	0.58

[1]Lag time ($t_{0,PIA}$ - $t_{0,CA}$) derived from non-linear fit (see Supplementary Information, section 2). [2]Experimental values for native rhodopsin. [3]Average hop time.

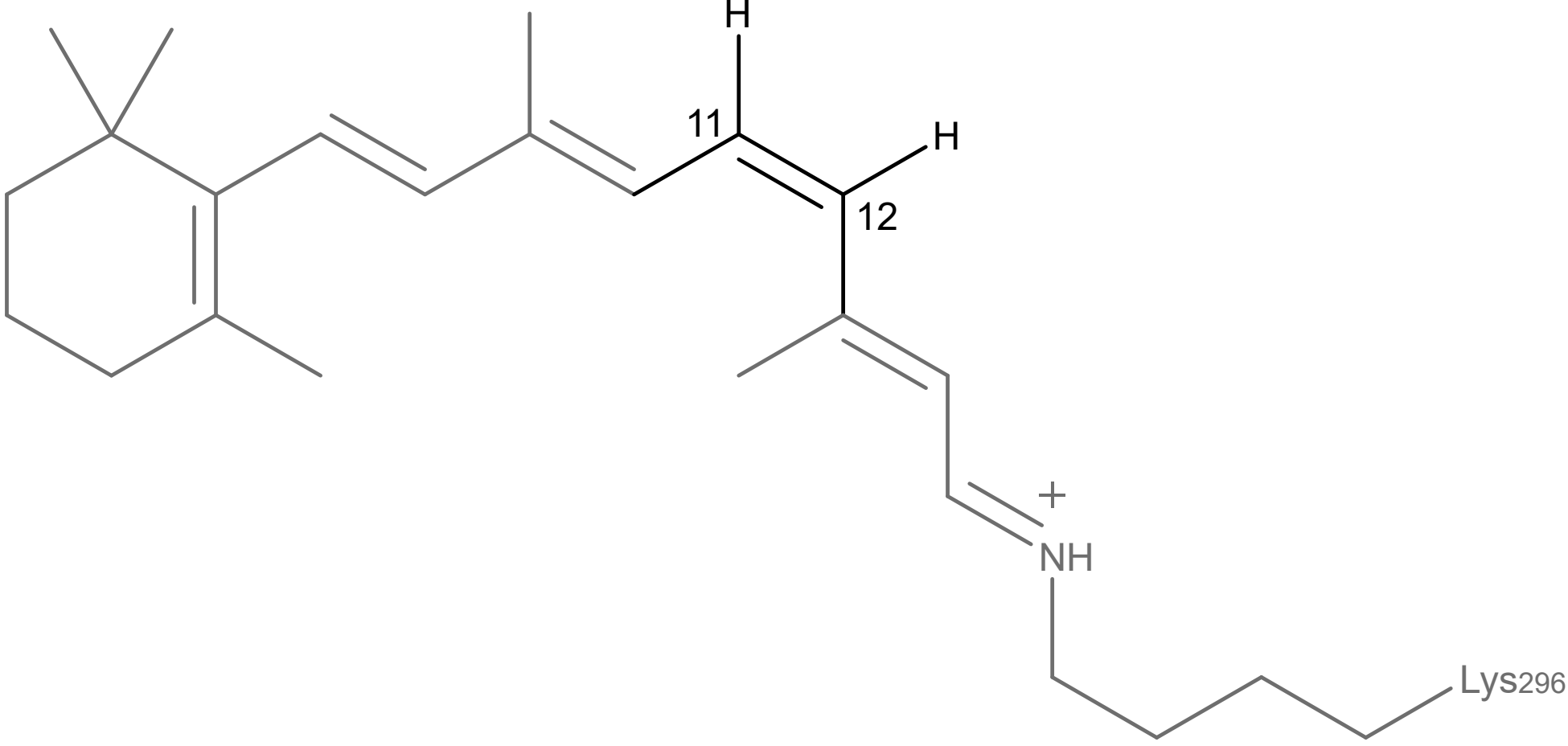

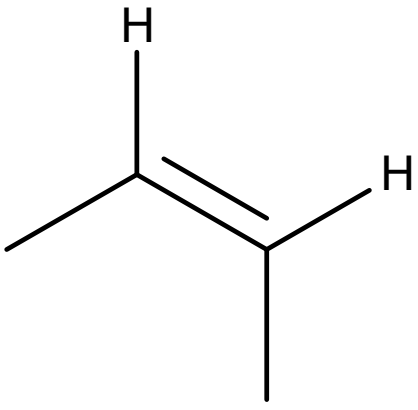

native rhodopsin

11,12-H_2 regenerated

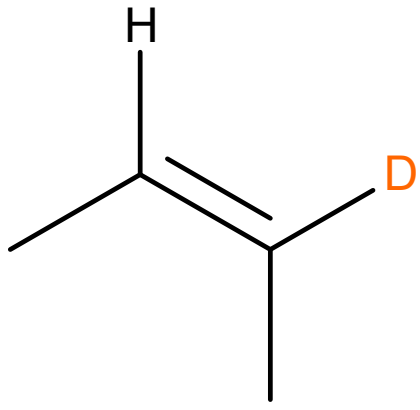

12-D

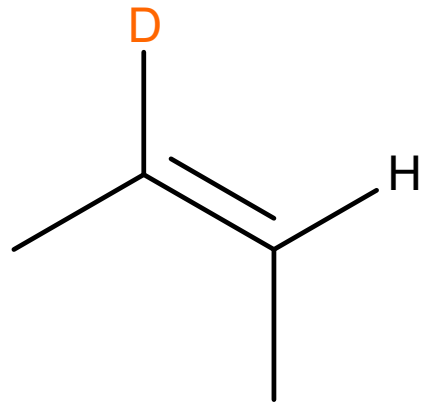

11-D

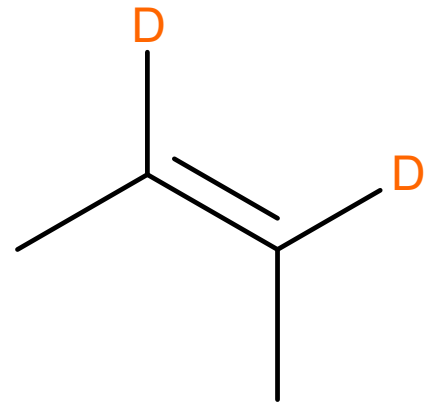

11,12-D_2

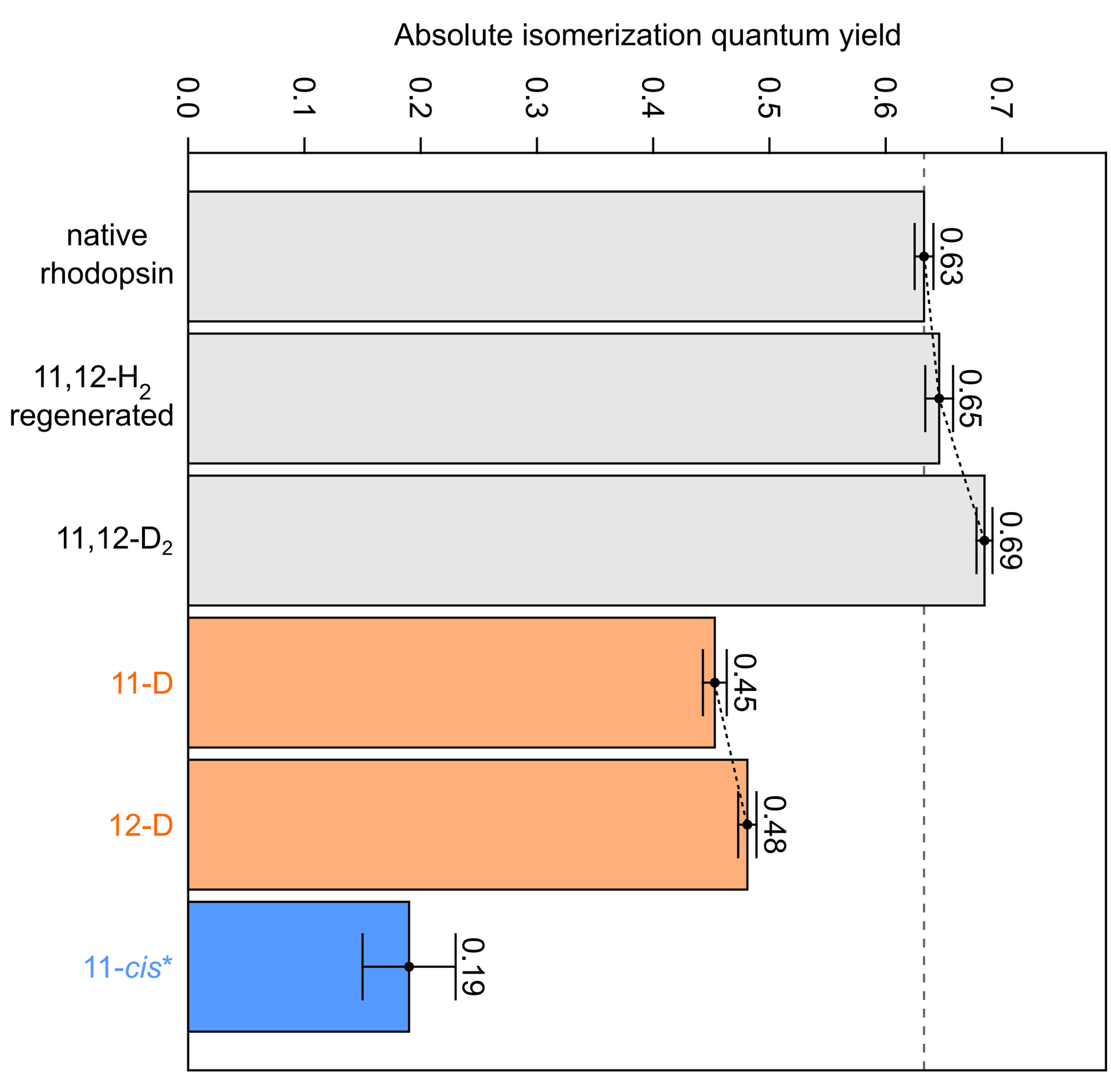
Absolute isomerization quantum yield
0.0
0.1
0.2
0.3
0.4
0.5
0.6
0.7
native rhodopsin
11,12-H2 regenerated
11,12-D2
11-D
12-D
11-cis*
0.63
0.65
0.69
0.45
0.48
0.19

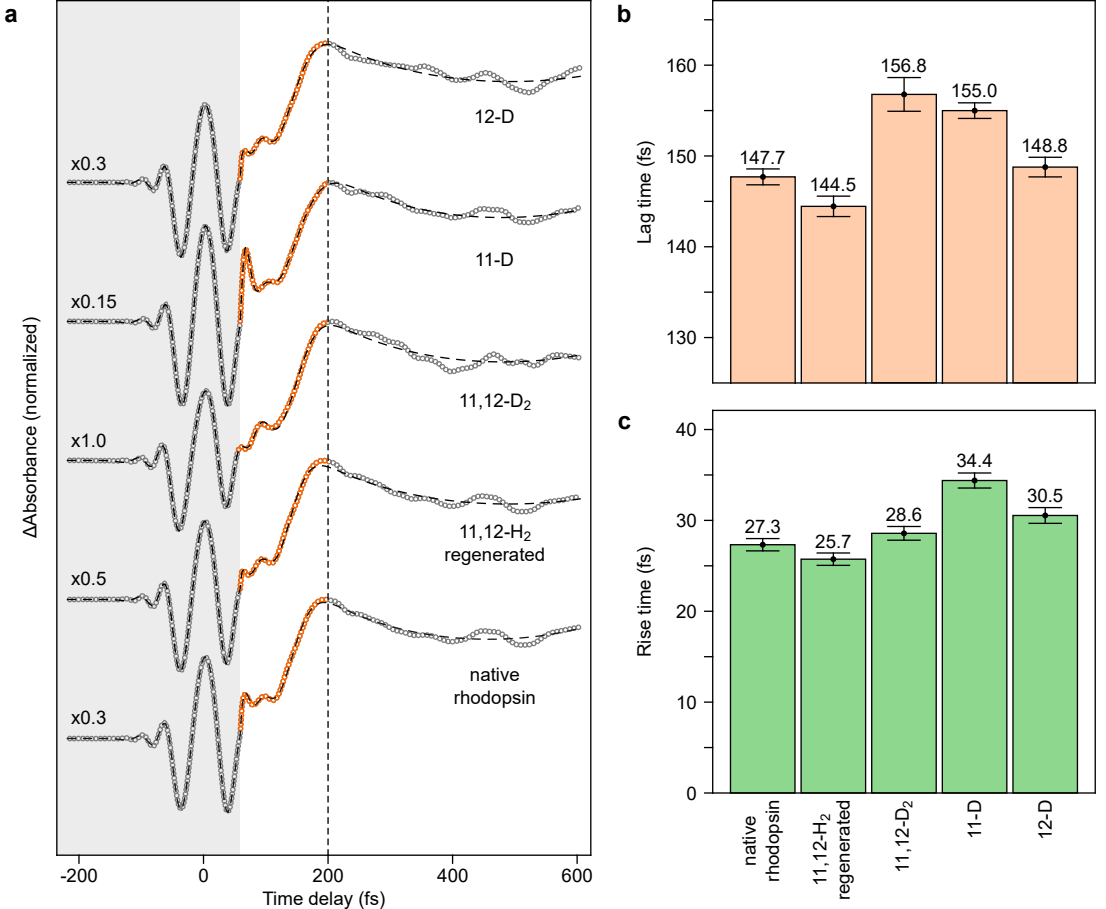
a
ΔAbsorbance (normalized)
x0.3
12-D
x0.15
11-D
x1.0
11,12-D2
x0.5
11,12-H2
regenerated
x0.3
native
rhodopsin
-200
0
200
400
600
Time delay (fs)
b
Lag time (fs)
130
140
150
160
147.7
144.5
156.8
155.0
148.8
c
Rise time (fs)
0
10
20
30
40
27.3
25.7
28.6
34.4
30.5
native rhodopsin
11,12-H2 regenerated
11,12-D2
11-D
12-D

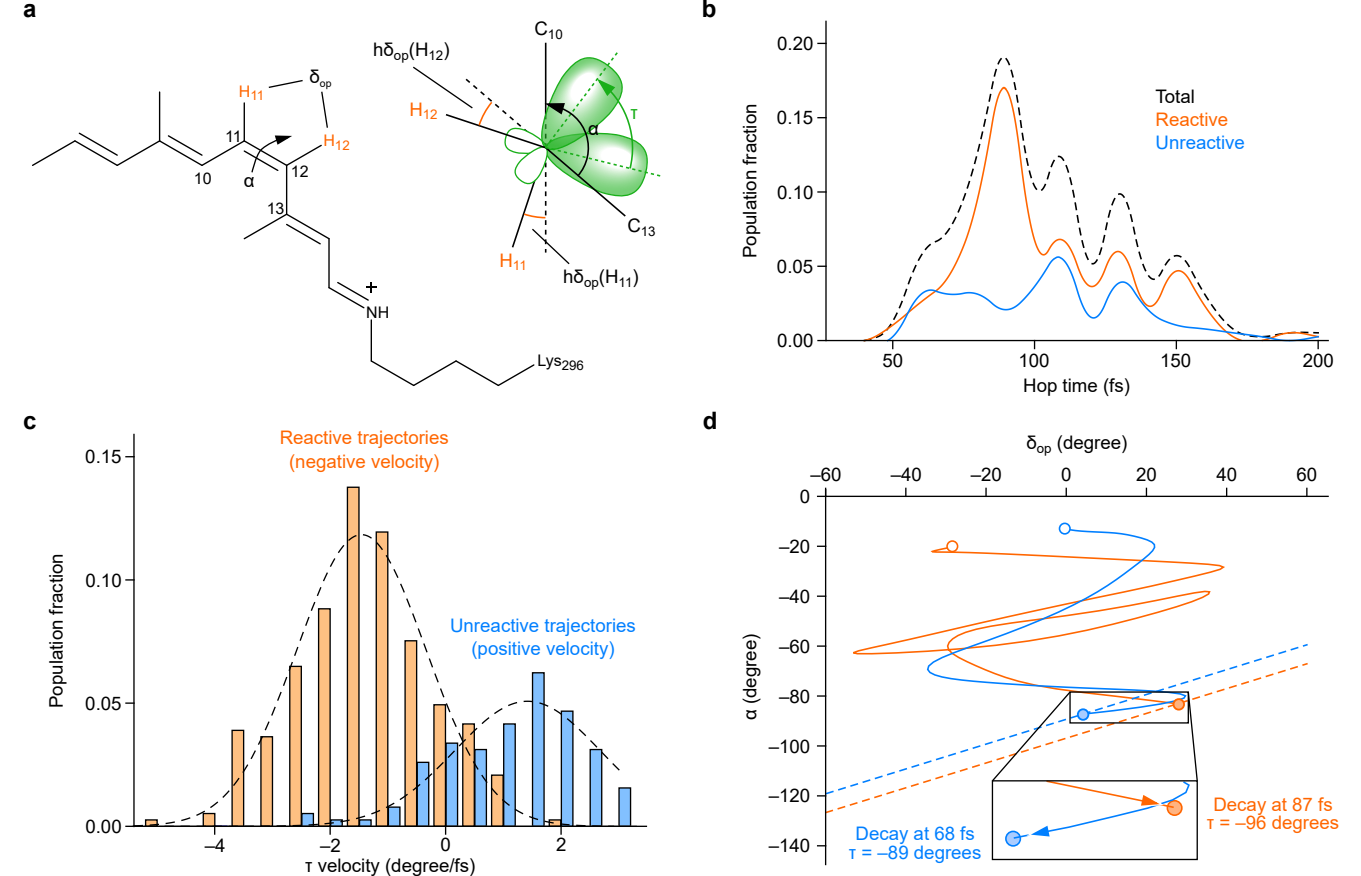
a
H11
δop
11
H12
10
α
12
13
+
NH
Lys296
hδop(H12)
C10
H12
τ
α
C13
H11
hδop(H11)
b
Population fraction
0.20
0.15
0.10
0.05
0.00
50
100
150
200
Hop time (fs)
Total
Reactive
Unreactive
c
Reactive trajectories
(negative velocity)
Unreactive trajectories
(positive velocity)
Population fraction
0.15
0.10
0.05
0.00
−4
−2
0
2
τ velocity (degree/fs)
d
δop (degree)
−60
−40
−20
0
20
40
60
α (degree)
0
−20
−40
−60
−80
−100
−120
−140
Decay at 68 fs
τ = –89 degrees
Decay at 87 fs
τ = –96 degrees

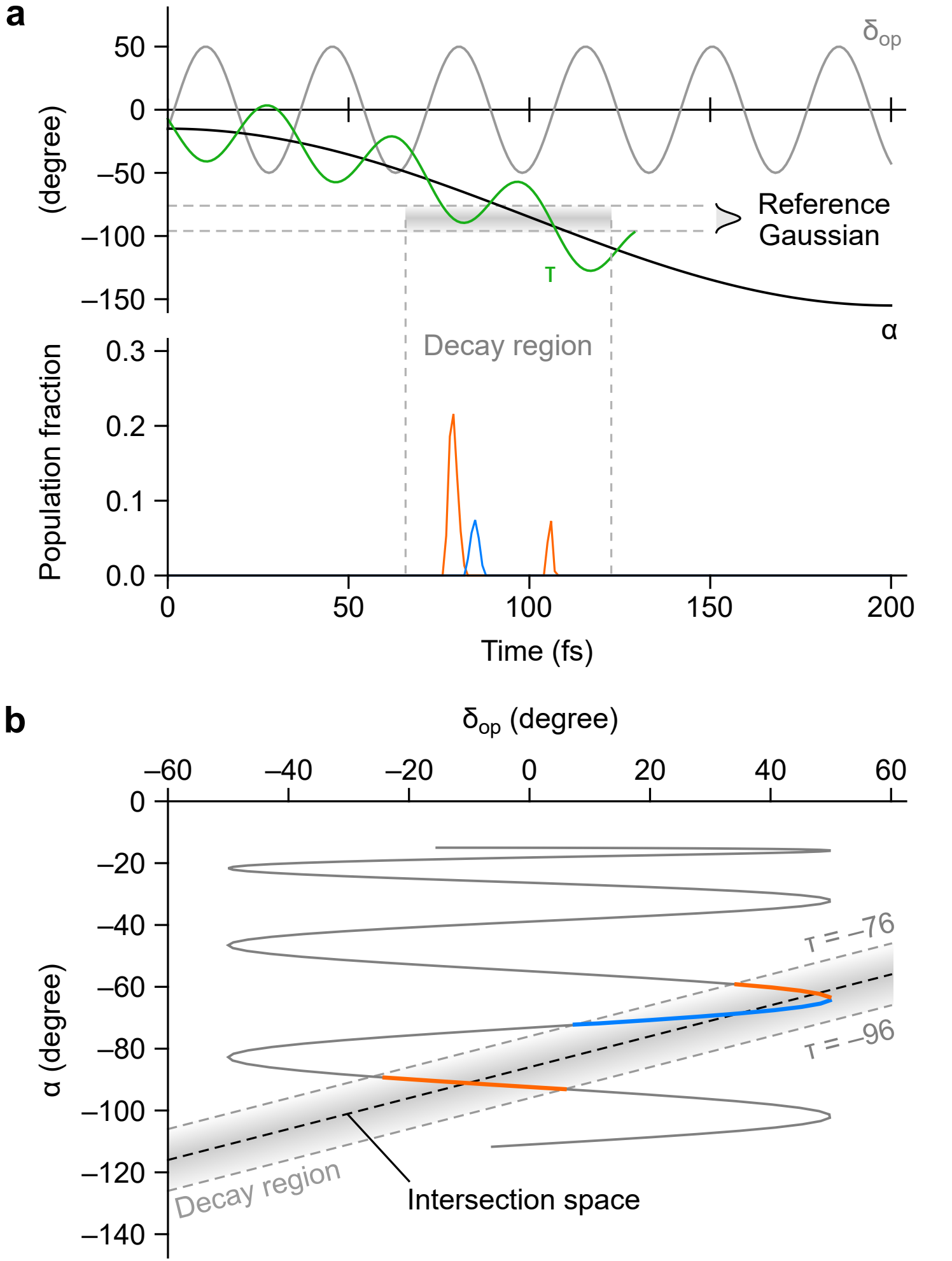
a
50
0
−50
−100
−150
(degree)
δop
Reference
Gaussian
τ
α
Decay region
0.3
0.2
0.1
0.0
Population fraction
0
50
100
150
200
Time (fs)
b
δop (degree)
−60
−40
−20
0
20
40
60
0
−20
−40
−60
−80
−100
−120
−140
α (degree)
τ = 76
τ = 96
Decay region
Intersection space